Dusty Lyman-alpha Emitters As Seen By Spitzer

A THESIS
SUBMITTED TO THE FACULTY OF THE GRADUATE SCHOOL
OF THE UNIVERSITY OF MINNESOTA
BY

Kyle Arthur Dolan

IN PARTIAL FULFILLMENT OF THE REQUIREMENTS
FOR THE DEGREE OF
MASTER OF SCIENCE

Claudia Scarlata

June, 2014

Acknowledgements

Special thanks to Peter Capak at the Spitzer Space Center, as well as Micaela Bagley, Michael Gordon, Mehdi Lame'e, Vihang Mehta, Karlen Shahinyan, and Dinesh Shenoy at the Minnesota Institute for Astrophysics.

Dedication

To all of my family and friends that have supported me over the years. Thank you for being there for me as I worked toward this goal.

Abstract

We present an analysis of *Spitzer* data for a large sample of low-redshift Lyα-emitting galaxies discovered by GALEX. Using the Donley et al. (2012) AGN selection region in color-color space IRAC photometry, we determined from our sample that the LAEs at $z \sim 0.3$ have an AGN fraction of $\approx 24\%$. The total bolometric $L_{\rm IR}$ for the sample was found using χ^2 fitting along with template SEDs, and we found that the galaxies ranged from $10^{8.05} L_\odot$ to $10^{11.57} L_\odot$, with a median $L_{\rm IR}$ value of $10^{10.39} L_\odot$. $L_{\rm IR}$ and $L_{\rm Ly\alpha}$ for our sample do not appear to be correlated, unlike the high-$L_{\rm IR}$ Lyα-emitting objects examined by Colbert et al. (2006) and Nilsson & Møller (2009), which may mean that their samples of LAEs, with $L_{\rm IR}/{\rm L}_\odot > 10^{12}$, are qualitatively different from our own. The SFR values for the sample have a median value of 5.63 $M_\odot$ yr^{-1}, in agreement with the value of $\sim 6 M_\odot$ yr^{-1} found in Cowie et al. (2011). Also, we find that most of the sample has a contribution of $SFR_{\rm IR}$ to $SFR_{\rm Total}$ that is greater than 60%, indicating that these LAEs have a significant amount of dust extinction, and SFR_{UV} alone is also not a good indicator for $SFR_{\rm Total}$. From comparing dust extinction to UV continuum slope β, it was found that LAEs do not follow the same curves predicted for SF or SB galaxies, indicating that LAEs at low redshift may experience more variation in their native UV spectra, making it impossible to recover their dust attenuation from their UV slope. This would suggest that LAEs may consist of stellar populations of varying ages, leading to more intrinsic variation in their UV slope.

Contents

List of Tables

List of Figures

Chapter 1

Introduction

The observation and study of the Lyα emission line is indispensable to our understanding of the high-redshift universe. At very high redshift ($z > 6$), this is the only spectroscopic signature that can be used to confirm the redshifts for galaxies, and often, Lyα observation is responsible for the discovery of the most distant galaxies. As an effective tracer of the faintest sources at the highest redshifts, Lyα also has the potential to help constrain the epoch of reionization, as a sharp drop in their number density is predicted as the intergalactic medium (IGM) changes to its ionized state sometime before $z \sim 6$ (Malhotra & Rhoads (2006), Miralda-Escude & Rees (1998)).

The ultraviolet Lyα line, however, is resonantly scattered by neutral hydrogen, so it is highly sensitive to the relative kinematics and geometry of dust and gas in the interstellar medium. Thus, our understanding of the intrinsic properties of Lyα emitters necessitates study of the relationships between a galaxy's Lyα emission and its star formation rate, dust extinction, luminosity, and spectral energy distribution. These kinds of studies are not possible for Lyα emitters (LAEs) at high redshift, because optical emission lines, infrared tracers of dust emission, and other relevant characteristics of distant galaxies are redshifted into expensive and inaccessible wavelength ranges.

Deharveng et al. (2008), however, as well as Cowie et al. (2011), have each found about 100 LAEs at $z \sim 0.2 - 0.4$ using the *Galaxy Evolution Explorer* (GALEX), which allows for a more complete study of LAEs. Low-redshift LAEs have the advantage of being bright and easily studied at longer wavelengths, which allows us to do statistical analysis on their physical properties and compare them to those of other local galaxies

(Oteo et al. (2012)). Of particular interest to us is that a large portion of these galaxies has been detected by *Spitzer*, making it possible to study the dust emission, extinction, SFR, and AGN contamination of LAEs more completely than has been done before.

In this paper, we use *Spitzer* data to study a larger sample of LAEs than has been previously available, deriving their infrared SEDs, rate of dust extinction, and the portion of star formation within the LAEs that is not recovered by UV and optical observations. The IRAC instrument on *Spitzer* also allows us to identify possible obscured AGN activity because, in galaxies that have a dusty torus surrounding the nucleus, the high-energy photons from the AGN are absorbed and re-emitted in the infrared, allowing the host galaxy to dominate the optical spectrum. By making an infrared study of these galaxies, we can identify which LAEs show the characteristic power-law spectrum in their dust emission, which we expect to see from AGN.

In Chapter 2, we describe our data set as well as the criteria we used to decide which galaxies to include in our study. In Chapter 3.1, we explain the methods we used to determine which of the LAE sample are likely to be obscured AGN, and in Chapter 3.2, we describe how we calculated the total bolometric (8μm-1000μm) IR luminosities for the galaxies in the sample. Chapter 4.1 shows how we determined the AGN fraction for our sample; Chapter 4.2.1 gives our analysis of their IR and UV luminosities; Chapter 4.2.2 shows our measured SFRs; and in Chapter 4.2.3 we investigate the relationship between dust attenuation and UV continuum slope for our data.

Chapter 2

Data

We started with the sample of 115 low-redshift LAEs discovered by Deharveng et al. (2008), and added to it from a sample of 91 objects analyzed by Cowie et al. (2011). The combined sample sets yielded a total of 142 unique objects. The galaxies are located in the CDF-South, ELIAS-S1, GROTH, COSMOS, SIRTFFL, and NGPD fields, and their redshifts fall in a range of values from $z = 0.176$ to $z = 0.468$, with a median redshift of $z = 0.2651$.

The images we used were collected by the *Spitzer* space telescope, using the IRAC (3.6, 4.5, 5.8, and 8.0μm) and MIPS (24, 70, and 160μm) instruments, and reduced using the MOPEX software package. The reduced data were made available as supermosaics in the Spitzer Heritage Archive, along with coverage maps and uncertainty maps. We found, in determining σ for the images (see below), that the IRAC (MIPS) images have a 3σ depth of approximately 22 (23) in the AB magnitude scale, using a 4.8" (7.0") diameter circular photometric aperture. We used the reduced data from the four IRAC channels and the MIPS 24μm channel for analysis, but excluded the 70μm and 160μm MIPS channels from this study because they have too large of a PSF for us to differentiate the sample objects from their neighbors. For our detection and analysis of each galaxy, we used a square cutout image, or "postage stamp", centered on the galaxy and covering an area of the sky 2' on a side. Of the 142 objects in our original sample, 137 objects had images available in the Spitzer archive.

We obtained $L_{\rm UV}$ and $L_{\rm Ly\alpha}$ for galaxies in our sample from data made available in Cowie et al. (2011). In all of our analysis comparing $L_{\rm IR}$, $L_{\rm Ly\alpha}$, and $L_{\rm IR}$ below, we used

only the newest UV and Lyα set available for our galaxies, reported in Cowie et al. (2011). The data set in Cowie et al. (2011) provides $L_{\mathrm{Ly}\alpha}$ and L_{UV} data for 77 galaxies in our list of 142 LAEs, so these are the galaxies we consider for our luminosity analysis in Chapter 4.2. In the Cowie et al. (2011) sample, they express L_{UV} as νL_ν and define it as the bolometric UV continuum luminosity above 1216 Å.

Chapter 3

Data Analysis

Using SExtractor software in dual-image mode, we detected all of the infrared sources in the vicinity of the GALEX coordinates for the LAEs. We assigned an IRAC and/or MIPS counterpart for each GALEX object, where possible, and measured the fluxes enclosed by circular photometric apertures centered on each object's SExtractor-defined coordinates. We used apertures of diameter 4.8" in all IRAC channels and 7.0" in the MIPS 24μm channel, applying the appropriate aperture corrections given in the IRAC and MIPS instrument handbooks.

For each GALEX object, we defined an infrared source as its counterpart if the SExtractor-defined coordinates matched the GALEX coordinates within a pre-determined tolerance. An IRAC source was defined as a GALEX object's counterpart if it was the only detected source within 3" of the GALEX coordinates in the 3.6 μm IRAC channel, and MIPS sources needed to be within 6" of the GALEX coordinates to be defined as the object's IR counterpart. If another infrared source was found within 3" (6") of the SExtractor-defined coordinates for a GALEX object's IRAC (MIPS) counterpart, it was flagged as having a neighboring object, and marked as such in any subsequent analysis (see below). In addition, if the GALEX coordinates appeared directly between two IR sources, or if an IR source could not be deblended from its neighbors, we assigned no counterpart and excluded the object from our analysis. In some cases with MIPS images (For example, with GALEX143720+344527), a source could not be extracted by SExtractor, but still was apparent from viewing the image. In this case, we used IDL to measure the flux at the GALEX coordinates for the object.

To measure the IRAC and MIPS flux errors, we avoided using SExtractor because SExtractor tends to underestimate photometric uncertainties for Spitzer data. This is largely because the software does not account for correlated noise or Spitzer calibration uncertainty (Gawiser et al. (2006), Barmby et al. (2008), Donley et al. (2012)). Instead, using the uncertainty maps provided by the Spitzer archive, we determined the uncertainties using square photometric apertures in IDL, 4.8" on a side for IRAC, and 7.0" for MIPS 24μm, and rescaled the resulting uncertainty measurements to be consistent with the photometric errors measured within circular apertures. Also, because the calibration errors for the Spitzer instruments may be as high as ten percent, if the photometric error for any flux measurement was calculated to be less than ten percent of the measured flux value, we redefined the error for that measurement to be ten percent of the flux.

We defined objects as non-detections if they had a flux of less than 3σ above the background flux, where σ is the uncertainty derived for each object's stamp. The value of σ was found by measuring the flux enclosed by 5000 randomly-placed circular photometric apertures on each image. We required each aperture to have no more than ten percent of its pixels contributed by a source, as defined by the segmentation maps derived by SExtractor. We fit a Gaussian profile to the histogram of the background flux values measured within all of the apertures, for each image stamp (See Figure A). The value of σ for each best-fit Gaussian curve was defined to be σ for flux values measured within each stamp.

3.1 Selection of AGN

To determine which of the galaxies in our sample are likely to contain AGN, we plotted the objects from our sample in [8.0μm-4.5μm] vs [5.8μm-3.6μm] color space (see Figure B). From the subset of our complete list of 142 objects that was not excluded from analysis due to lack of data, inability to assign a single IR counterpart, or non-detection, we found that 54 objects were above the 3σ detection limit in all four IRAC channels (See Table A.1). Also, 18 objects (See Table A.2) were detected in enough IRAC bands to be constrained in one of the two dimensions on the IRAC color-color plot, and are shown as limits (Lacy et al. (2007), Stern et al. (2005)).

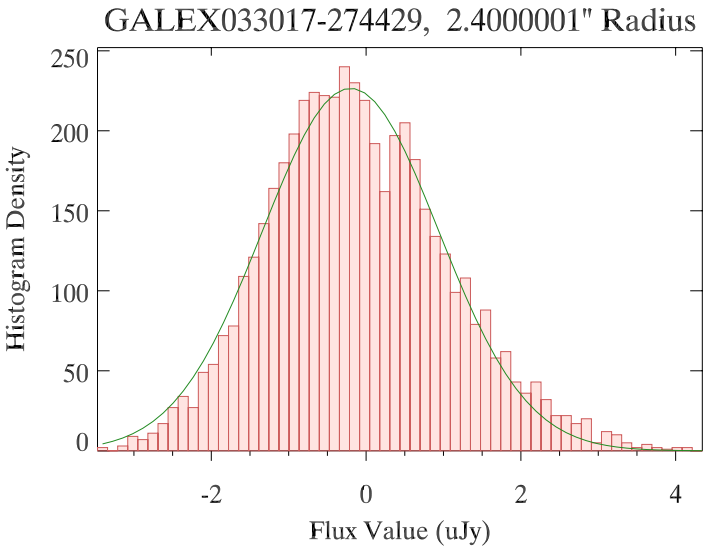

Figure A One of the histograms used to define the background σ for each object, in each *Spitzer* channel. The plot above is for the IRAC 3.6μm channel, and the histogram shows the flux enclosed by randomly-placed photometric apertures of radius 2.4", the same size as the photometric apertures used to measure the IRAC flux for each object. The green curve is a Gaussian that we fit to the histogram, giving us a σ value, for this object, of ≈ 1.139 μJy in the 3.6μm channel, and a 3σ detection limit of ≈ 3.416 μJy.

We used two selection regions in our color-color plot to indicate the likelihood that a galaxy contains an AGN: The Lacy et al. (2007) region (shown in black), sometimes called a "Lacy Wedge"; and the Donley et al. (2012) selection region (shown in red), which is a refinement of the region defined in Lacy et al. (2007). To check the reliability of the selection regions and show the pattern that galaxies of different spectral types will form in color-color space, we also plot synthetic IRAC color-color data points, created using the Swire template database provided by Polletta et al. (2007) (See Table 3.1). To illustrate the distribution of our sample in redshift space, as well as to show how galaxies change position in color-color space with changing redshift, we split the sample into two redshift bins, one with $z \leq 0.3$ and one with $z \geq 0.3$. For the lower redshift bin, the Swire template objects are redshifted to $z = 0.25$, and for the higher redshift bin, the template objects are redshifted to $z = 0.35$. As Figure B shows, even a small change in redshift noticeably alters the positions of the template galaxies on the color-color plot.

Table 3.1: – The SWIRE Spectral Library

Template	Spectral Type
Ell2	Ell (t=2 Gyr)
Ell5	Ell (t=5 Gyr)
Ell13	Ell (t=13 Gyr)
S0	Spiral 0
Sa	Spiral a
Sb	Spiral b
Sc	Spiral c
Sd	Spiral d
Sdm	Spiral dm
Spi4	Spiral c
NGC6090	Starburst
M82	Starburst
Arp220	Starburst/ULIRG
IRAS 20551-4250	Starburst/ULIRG
IRAS 22491-1808	Starburst/ULIRG
NGC 6240	Starburst/Seyfert 2
Sey2	Seyfert 2
Sey1.8	Seyfert 1.8
IRAS19254-7245 South	Seyfert 2 + Starburst/ULIRG
QSO2	Type 2 QSO
Torus	Type 2 QSO
Mrk231	Seyfert 1, BAL QSO, Starburst
QSO1	Type 1 QSO
BQS01	Type 1 QSO
TQS01	Type 1 QSO

The Donley et al. (2012) AGN selection region starts with a selection box defined by $\alpha \leq -0.5$ (where the spectrum of an AGN is expected to fit a power law function of the form $\log f_\nu = \alpha \log \nu + b$), which appears as a diagonal rectangular region in color-color space. The authors make a further vertical cut to exclude low-redshift, star-forming galaxies from the selection region, and a horizontal cut to prevent contamination from galaxies with $z \geq 2$ that are bright enough to be included in the COSMOS IRAC sample. For our purposes, the power law selection box and vertical cut are most influential in the selection of likely AGN from our sample.

Even though the Lacy Wedge does contain several Seyfert template galaxies that are not contained by the Donley region (see Figure B), the region defined in Donley et al. (2012) was found to be preferable to the Lacy Wedge because it avoids contamination by normal star-forming galaxies and starburst galaxies. As Figure B shows, the Lacy Wedge also contains several starburst template galaxies, some of which appear in nearly the same places as the Seyfert template galaxies. Donley et al. (2012) found that the probability of a galaxy being an AGN was, at best, $\sim 10\%$ to $\sim 20\%$ if it was located inside the Lacy Wedge but not in the new selection region.

3.2 Luminosity

To determine each galaxy's bolometric $L_{\rm IR}$ $(8 - 1000\mu{\rm m})$, we used χ^2 fitting to find a best-fit spectral energy distribution (SED) for each galaxy's measured flux values (in rest-frame wavelength). We used the set of 105 template SEDs presented by Chary & Elbaz (2001) (Hereafter referred to as CE01). For each of the objects, we fitted the template spectra to the measured luminosity density, L_ν, for the four IRAC bands and the MIPS 24μm band. For each measured flux density f_ν defined in units of ergs ${\rm s}^{-1}{\rm cm}^{-2}{\rm Hz}^{-1}$, the luminosity density L_ν was calculated as

$$L_\nu = \frac{4\pi {D_L}^2 f_\nu}{1+{\rm z}} \tag{i}$$

where D_L is the luminosity distance, in centimeters, for an object at redshift z in a $H_0 = 73$ km s^{-1} Mpc^{-1}, $\Omega_{\rm M} = 0.3$, $\Omega_\Lambda = 0.7$ cosmology.

For each object i, we found the CE01 template k which yielded the minimum value for ${\chi_{i,k}}^2$, where ${\chi_{i,k}}^2$ is defined as

$${\chi_{i,k}}^2 = \sum_{j=1}^{5} \frac{\left(O_{i,j} - A_{i,k}E_{i,j,k}\right)^2}{\sigma^2} \tag{ii}$$

where $O_{i,j}$ is the observed luminosity density L_ν at rest-frame wavelength j, $E_{i,j,k}$ is the luminosity density of the kth SED at the same rest-frame wavelength, and $A_{i,k}$ is a normalization factor, calculated to be

$$A_{i,k} = \frac{\sum_{j=1}^{5} \frac{(O_{i,j}\cdot E_{i,j,k})}{\sigma^2}}{\sum_{j=1}^{5} \frac{{E_{i,j,k}}^2}{\sigma^2}}. \tag{iii}$$

Note that each of the sums above is over all five rest-frame wavelengths we fitted, unless a given object is undetected in one or more of those wavelengths. In that case, those wavelengths are left out of the sums when we calculate ${\chi_{i,k}}^2$. For each galaxy, we calculated ${\chi_{i,k}}^2$ for each of the 105 CE01 templates and selected the best value of ${\chi_{i,k}}^2$ out of those 105 values as our best fit.

As the top example shows in Figure C, we found best-fit templates for all of the objects that were detected in all five *Spitzer* wavelengths we were using. When an object was undetected in one or more of our *Spitzer* channels, as shown in the bottom example, we adjusted the selection criteria of the χ^2 fitting so that the best-fit template had to have L_ν less than the upper limit for the undetected wavelength(s) to be selected as a fit. As a result, whenever an object was undetected in one or more *Spitzer* channels, the value of χ^2 could rise, preventing us from constraining $L_{\rm IR}$ as well as we could for fully detected objects.

Once we found the best-fit template SED for each object, we used the integrated $L_{\rm IR}$ values provided by Charie & Elbaz (2001) for each of their templates, scaling the values using the normalization factor $A_{i,k}$ given in Equation iii.

In order to determine the degree of uncertainty for the $L_{\rm IR}$ values we derived via SED fitting, we also derived error bars using randomized, synthetic values for L_ν. Using the known error bars for each measured value of L_ν in each wavelength, we produced 1000 instances of synthetic photometry for each object. In each instance, we generated values for $L_{\nu,j}$ at random, between the top and bottom error bars for each wavelength. For each instance of synthetic photometry, we performed the same χ^2 fitting procedure described above. Then, for each object, we constructed a histogram of the resulting synthetic, randomized values for $L_{\rm IR}$(See Figure D).

Treating the resultant distributions of $L_{\rm IR}$ values as pseudo-normal distributions, we then define the error bars for $L_{\rm IR}$ to be placed at $L_{\rm IR}+\sigma$ and $L_{\rm IR}-\sigma$. Following the statistics for normal distributions, $L_{\rm IR}+\sigma$ is the point on the histogram distribution that is greater than 84% of the other synthetic $L_{\rm IR}$ values, and $L_{\rm IR}-\sigma$ is the point that is greater than 16% of the next-highest $L_{\rm IR}$ values, as is marked in Figure D.

For our luminosity analysis in Section 4.2 below, we exclude any objects for which we cannot effectively constrain $L_{\rm IR}$, using the method above. Objects could not be effectively constrained if they did not yield a detection in enough IRAC channels; if

they could not be deblended from their neighbors using SExtractor; if the $L_{\rm IR}$ error bars generated for the objects failed to encompass the $L_{\rm IR}$ values we derived from their detections; or if they could not be assigned a single counterpart in the *Spitzer* channels. Non-detection of an object in the IRAC 5.8μm and/or 8.0μm wavelengths was the most common lack of detection that we encountered, and this led to poorly-constrained $L_{\rm IR}$ values because those wavelengths are in the regime of dust emission, which is the main source of the infrared light that wish to detect. Likewise, when the MIPS 24μm contribution for an object was undetected or unavailable, it was also more difficult to constrain the dust emission, giving us an poorly constrained value of $L_{\rm IR}$. Overall, excluding all such poorly-constrained objects, we have a total of 48 objects remaining that are detected, effectively constrained in terms of $L_{\rm IR}$, and represented in the data set from Cowie et al. (2011).

For the objects whose $L_{\rm IR}$ could not be constrained via SED fitting, if we have a MIPS 24μm limit or detection for them, we use those MIPS 24μm values to define their $L_{\rm IR}$ as an upper limit, using the average $L_{\rm IR}$ values for low-redshift LAEs determined by Lee et al. (2011).

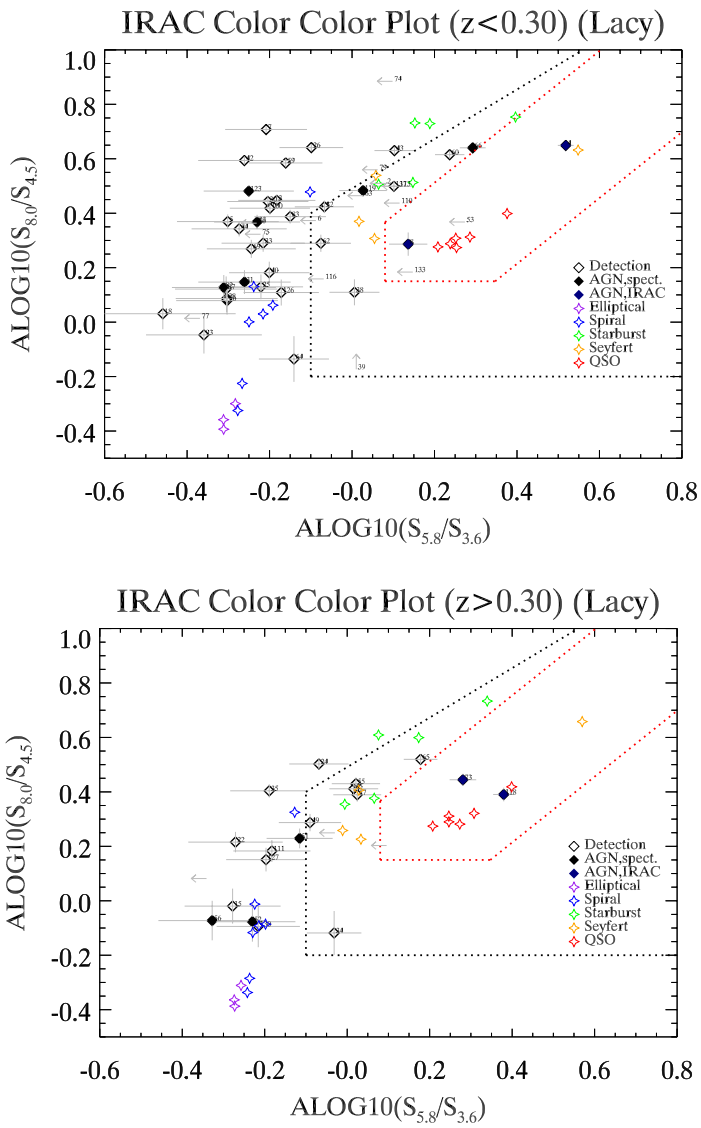

Figure B Color-color plots showing the AGN selection regions of Lacy et al. (2007) (black dotted line) and Donley et al. (2012) (red dotted line). Black open diamonds are galaxies detected in all four IRAC bands, while limits are shown as gray arrows. Black filled diamonds are galaxies confirmed to be AGN by spectroscopic observation. Dark blue filled diamonds are AGN identified using the Donley AGN selection region. The colored diamonds are synthetic IRAC color-color data points generated using the Polletta et al. (2007) template spectra, redshifted to $z = 0.25$ (first plot) and $z = 0.35$ (second plot). The template objects include elliptical galaxies (purple), spiral galaxies (blue), starburst galaxies (green), Seyfert galaxies (orange), and QSOs (red).

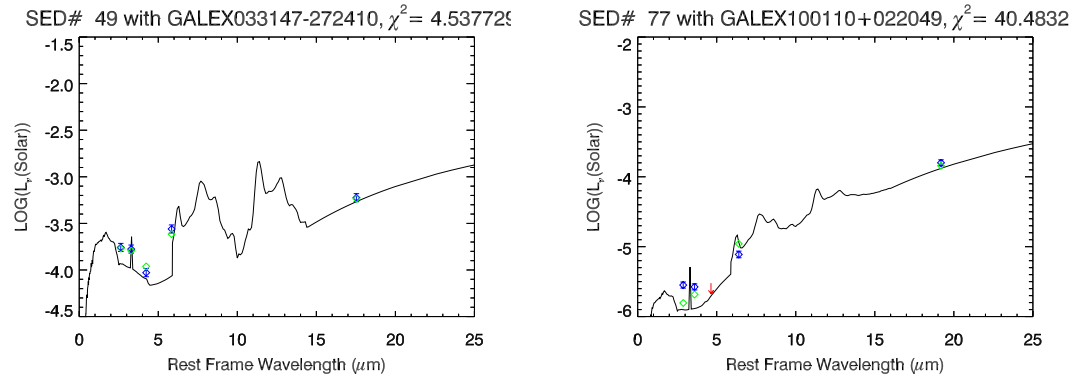

Figure C Two examples of the χ^2 template SED fitting used to find the bolometric $L_{\rm IR}$ for our sample galaxies. The green diamonds indicate what L_ν values *Spitzer* would detect for a galaxy with an SED identical to that of the template SED shown here. Note that, in the second object, the IRAC 5.8μm luminosity density was below the 3σ detection limit. The best-fit template SED was selected taking this limit into account, resulting in a template with a higher value for χ^2 .

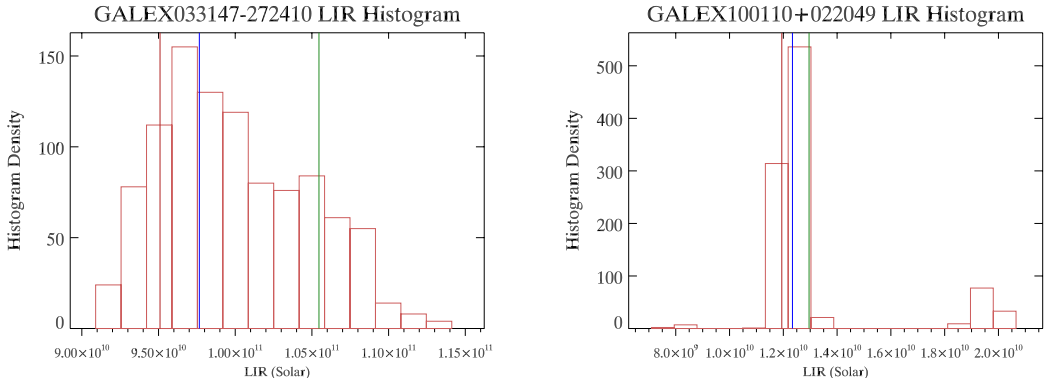

Figure D Two histograms showing the randomized synthetic $L_{\rm IR}$ values we produced to estimate the errors for $L_{\rm IR}$. The blue line indicates the value for $L_{\rm IR}$ derived from the *Spitzer* data, whereas the red line and the green line indicate $L_{\rm IR}$ values from the randomized synthetic data that are 1σ below and above the derived value, respectively. Note that the second histogram apparently has two peaks, indicating that, some of the randomized synthetic data, a different SED template may be a better fit, producing a different $L_{\rm IR}$value.

Chapter 4

Results

4.1 AGN Fraction

In the first redshift bin of our IRAC color-color plot ($z \leq 0.3$), we have 36 detections and 14 limits. Six AGN have already been confirmed as such in the literature, through the use of optical spectroscopy (shown as black diamonds). Using IRAC color-color space, which allows us to use the infrared spectra of galaxies to identify likely AGN, we identify two more AGN (shown as dark blue diamonds), well within the Donley et al. (2012) AGN selection region (See Figure B). One galaxy appears close to a Seyfert template galaxy and the closest neighbors of the other are QSO template galaxies. Notably, five other galaxies appear in the "Lacy Wedge" but not in the Donley region, so according to Donley et al. (2012), these galaxies are more likely to be star-forming galaxies that have contaminated the Lacy Wedge. We therefore identify these galaxies as Low-Likelihood AGN Candidates, or simply LLACs.

In the second redshift bin ($z \geq 0.3$), we have only 13 detections and 4 limits, which shows a predictable selection bias (fewer objects are detected at larger distances). Of the detections, three are known to be AGN from the literature, and two more are flagged as AGN due to their position in color-color space, located well within the Donley AGN selection region. The spectral types of these galaxies' closest neighbors from the template list, and thus their most likely spectral type, is QSO. Six other detections are within the Lacy et al. (2007) AGN region, but outside the Donley selection region. Their closest neighbors from the template list are starburst, Seyfert, or spiral galaxies,

so we cannot determine from color-color space alone, whether or not they are AGN. Therefore, we identify these galaxies as another subset of LLACs.

Overall, combining spectroscopically confirmed AGN and AGN found using the Donley AGN selection region, we have a total of 13 AGN (including one new likely Seyfert and three new likely QSOs) in our sample of 54 fully-detected galaxies, or ≈24% AGN. Given that the AGN fraction is sensitive to variation due to our relatively small sample size, it is consistent with the results of previous works by Cowie et al. (2011) and Scarlata et al. (2009), who found AGN fractions of ≈ 20% and ≈ 17%, respectively. This result is much lower than the results of Finkelstein et al. (2009b), which found an AGN fraction of $\approx 43^{+18}_{-26}\%$, although the very large error bars on this result do enclose our own result here.

4.2 Luminosity Analysis

The $L_{\rm IR}$ measurements that we made from the *Spitzer* data, along with the $L_{\rm UV}$ data provided in Cowie et al. (2011), represent the re-emitted light that was absorbed by dust in the UV, and the UV light that was able to escape each galaxy, respectively. We can use these luminosity measurements to analyze the physical properties of the galaxies in our sample. This section consists of our analysis of the 48 galaxies that are represented, both in our *Spitzer* data, and in the Cowie et al. (2011) data, and the physical properties of our sample that we are able to determine.

4.2.1 IR and UV Luminosity

The $L_{\rm IR}$ values that we obtained for our sample are shown in Figure A, along with the Lyα equivalent width values given in Cowie et al. (2011). Our sample ranges in $L_{\rm IR}$ from $10^{8.05}L_\odot$ to $10^{11.57}L_\odot$, with a median $L_{\rm IR}$ value of $10^{10.39}L_\odot$. Five of the galaxies qualify as Luminous infrared Galaxies (LIRGS) with $10^{11} < L_{\rm IR}/L_\odot < 10^{12}$, but none qualify as Ultra-Luminous infrared Galaxies (ULIRGS), which are defined as having $L_{\rm IR}/L_\odot > 10^{12}$. Thus, as was also found in Oteo et al. (2012), we find that more than 80% of LAEs at $z \sim 0.3$ fall in the $L_{\rm IR}$ range for normal, star-forming galaxies, with $L_{\rm IR}/L_\odot < 10^{11}$.

Interestingly, our $L_{\rm IR}$ plots show several objects with $L_{\rm IR}/L_\odot \lesssim 10^9$, each at least a

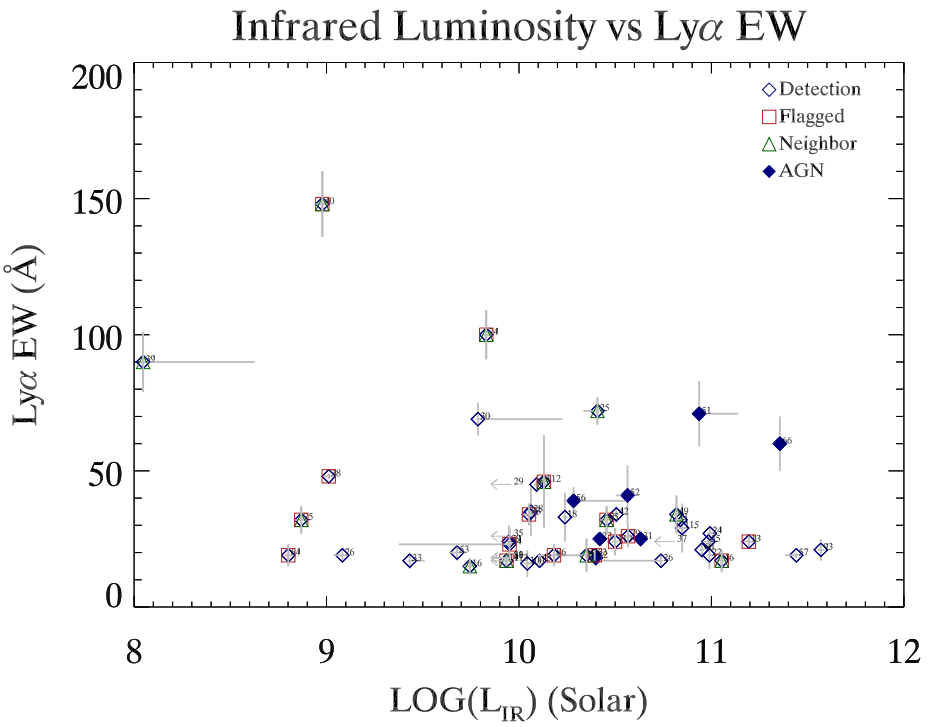

Figure A $L_{\rm IR}$ vs Lyα equivalent width, for our sample of low-redshift LAEs.

full order of magnitude less luminous than the least-luminous LAEs in the sample of 30 low-redshift LAEs analyzed in Oteo et al. (2012) (See Figure A). This is probably due to the fact that we have a larger sample of LAEs, allowing us to examine a wider range of luminosities for LAEs at $z \sim 0.3$.

In Figure B, we plot the derived $L_{\rm IR}$ values vs the $L_{\rm Ly\alpha}$ values supplied by Cowie et al. (2011). As Nilsson & Møller (2009) have found, we also see no correlation between $L_{\rm Ly\alpha}$ and $L_{\rm IR}$ in our low-redshift data. This indicates that at low $L_{\rm Ly\alpha}$ and/or $L_{\rm IR}$ values, the Lyα and IR properties of galaxies are unrelated. In contrast, Colbert et al. (2006) and Nilsson & Møller (2009) do see a loose correlation between $L_{\rm IR}$ and $L_{\rm Ly\alpha}$ for Lyα blobs at $z = 2.38$ and LAEs at $z = 2.3$. The blobs have a $L_{\rm Ly\alpha}/L_{\rm IR}$ ratio of $\approx 0.1\%$, shown in Figure B as a black dashed line, while the higher-redshift LAE galaxies show a ratio of $L_{\rm Ly\alpha}/L_{\rm IR} \approx 0.02\%$, shown as a purple dashed line. The correlation seen in high-$L_{\rm IR}$ objects by Colbert et al. (2006) and Nilsson & Møller (2009) may show

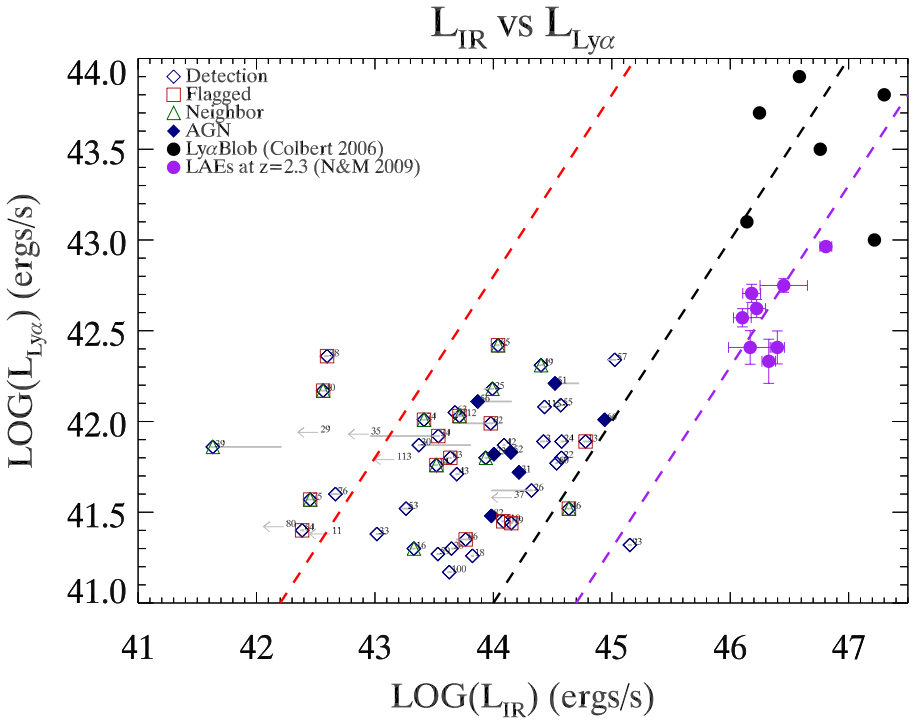

Figure B $L_{\rm IR}$ vs $L_{\rm Ly\alpha}$ for our sample of low-redshift LAEs, also including the known Lyα "Blobs" at $z = 2.38$ from Colbert et al. (2006). The dashed black line marks a $L_{\rm IR}/L_{\rm Ly\alpha}$ ratio of 0.1%, and the dashed red line marks the expected ratio from Case B, dust-free Lyα recombination, calculated to be 0.063%.

that at higher $L_{\rm IR}$ and/or $L_{\rm Ly\alpha}$ values, or at higher redshift, $L_{\rm IR}$ and $L_{\rm Ly\alpha}$ are more correlated. This could mean that the objects from Colbert et al. (2006) and Nilsson & Møller (2009) are qualitatively different from the objects in our own sample. The observed correlations, however, are based on small number statistics, and larger sample sizes would be necessary to confirm the observed relations.

The red dashed line Figure B is the expected ratio between $L_{\rm IR}$ and $L_{\rm Ly\alpha}$ in dust-free Case B recombination theory. We calculated this ratio using the latest Star Formation Rate (SFR) calibrations from Kennicutt & Evans (2012). The authors define star formation rate in terms of both $L_{\rm IR}$ and Hα as follows:

$$SFR_{\rm (IR)}[{\rm M}_\odot\ {\rm yr}^{-1}] = 3.89 \times 10^{-44} \times L_{\rm IR}\ [{\rm ergs\ s}^{-1}] \qquad \text{(i)}$$

$$SFR_{(\mathrm{H}\alpha)}[\mathrm{M}_\odot\ \mathrm{yr}^{-1}] = 5.37 \times 10^{-42} \times L_{\mathrm{H}\alpha}\ [\mathrm{ergs\ s}^{-1}] \quad \text{(ii)}$$

Thus, we can define the expected ratio between L_{IR} and $L_{\mathrm{H}\alpha}$ as

$$\frac{SFR_{(\mathrm{IR})}}{SFR_{(\mathrm{H}\alpha)}} = 0.0072, \quad \text{(iii)}$$

and given that the line ratio between Hα and Lyα is 8.7 for Case B recombination (Osterbrock & Ferland (2006)), we have that the expected ratio between $L_{\mathrm{Ly}\alpha}$ and L_{IR} is $\approx 6.3\%$, as the red dashed line in Figure B shows.

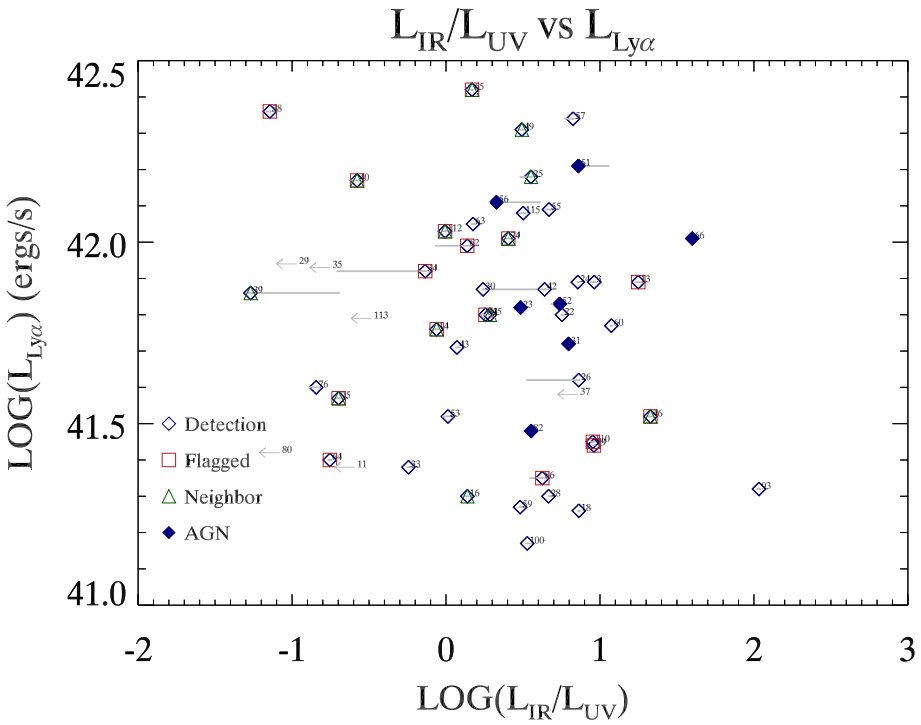

Figure C $L_{\mathrm{Ly}\alpha}$ vs the ratio between L_{IR} and L_{UV} for our sample of low-redshift, also including the Lyα "Blobs" from Colbert et al. (2006).

Several of the galaxies from our sample fall to the left of the red dashed line in Figure B, indicating that they have a higher $L_{\mathrm{Ly}\alpha}$ than we would calculate from their L_{IR} values in the case of dust-free, Case B recombination. Given, however, that these

galaxies are also the galaxies with the lowest $L_{\rm IR}$ values shown in Figure A, as well as having $L_{\rm IR}/L_{\rm UV}$ ratios that are all less than unity (See Figure C), we expect their total star formation rate, and thus their total $L_{{\rm Ly}\alpha}$, to also depend significantly upon their $L_{\rm UV}$ values. Thus, their high $L_{{\rm Ly}\alpha}$ values in Figure B are not surprising.

4.2.2 Star Formation

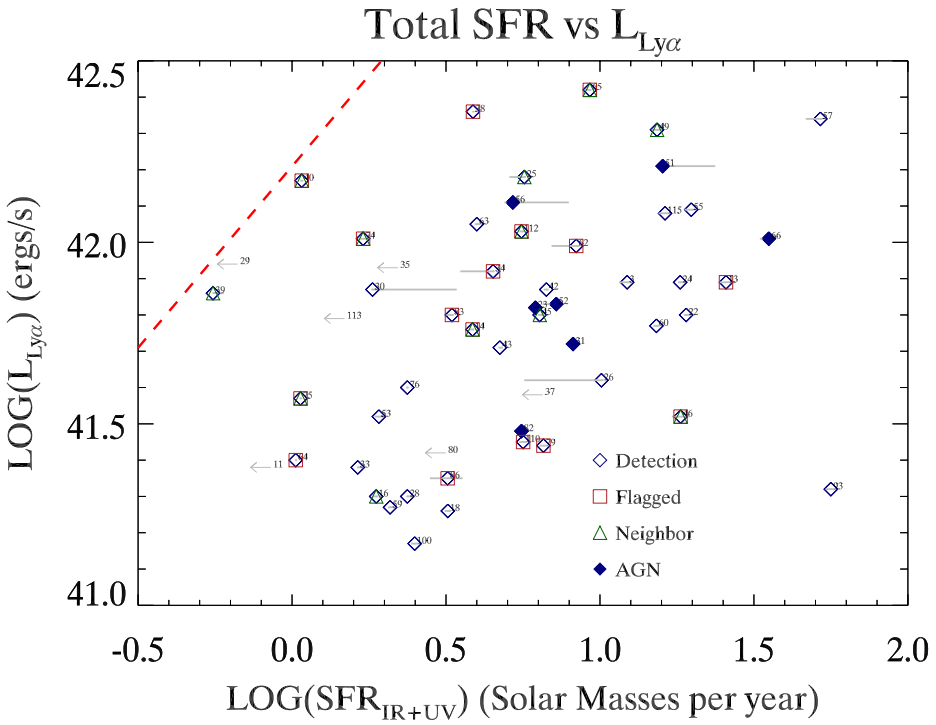

Figure D The $L_{{\rm Ly}\alpha}$ for our sample, against the total star formation rate calculated for UV and IR luminosities combined, using the updated SFR indicators from Kennicutt & Evans (2012). The red dashed line traces the $L_{{\rm Ly}\alpha}$/SFR ratio calculated for dust-free, Case B recombination, defined as 1.62×10^{42}.

To determine the total SFR for our sample of galaxies, we combine the $L_{\rm IR}$ and $L_{\rm UV}$ data, using Equation i above along with the following equation from Kennicutt & Evans (2012) :

$$SFR_{\rm (NUV)}[{\rm M}_\odot\ {\rm yr}^{-1}] = 6.76 \times 10^{-44} \times L_{\rm NUV}\ [{\rm ergs\ s}^{-1}] \qquad \text{(iv)}$$

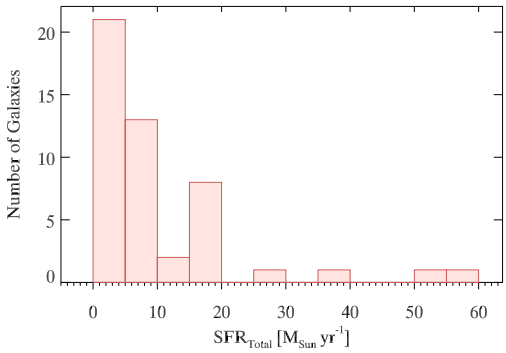

Figure E Distribution of $SFR_{\rm Total} = SFR_{\rm IR} + SFR_{\rm NUV}$ for our sample.

We define $SFR_{\rm Total}$ as $SFR_{\rm IR} + SFR_{\rm NUV}$ and plot $SFR_{\rm Total}$ vs $L_{{\rm Ly}\alpha}$ for our sample in Figure D, including the Lyα blobs from Colbert et al. (2006) and a red, dashed line showing the expected ratio between $L_{{\rm Ly}\alpha}$ and $SFR_{\rm Total}$.

This ratio was calculated using Equation ii, taking the inverse of $SFR_{({\rm H}\alpha)}$ and multiplying it by the Lyα/Hα ratio of 8.7, giving us a value of

$$L_{{\rm Ly}\alpha} = 1.62 \times 10^{42}\ [\text{ergs s}^{-1}] \times SFR_{\rm Total}[\text{M}_\odot\ \text{yr}^{-1}]. \qquad \text{(v)}$$

As is shown in Figure D, the galaxies' values for $SFR_{\rm Total}$ all fall to the right of the red dashed line, indicating that the $SFR_{\rm Total}$ values we have derived are all consistent with at least some dust extinction happening in each galaxy in the sample. The galaxies falling closest to the line include the low-$L_{\rm IR}$ galaxies discussed in Section 4.2.1, which would make sense as their very low $L_{\rm IR}/L_{\rm UV}$ ratios would be consistent with very low dust extinction.

Most of the galaxies in our sample have a value for $SFR_{\rm Total}$ less than 20 $M_\odot$ yr^{-1}, and the median value for $SFR_{\rm Total}$ is 5.63 $M_\odot$ yr^{-1}. The distribution peaks at around 3 $M_\odot$ yr^{-1} (See Figure E). Our median value is smaller than the median value of 18 $M_\odot$ yr^{-1} reported by Oteo et al. (2012), but it is consistent with the value reported in Cowie et al. (2011) using extinction-corrected Hα luminosities, $\sim 6 M_\odot$ yr^{-1}.

Figure F shows the ratio between $SFR_{\rm IR}$ and $SFR_{\rm Total}$, against $L_{\rm UV}$for our sample of LAEs. The wide range for this ratio shows us that for our sample, $SFR_{\rm IR}$ alone is not a good indicator of $SFR_{\rm Total}$. We find, however, that for 27 of the 48 galaxies in our

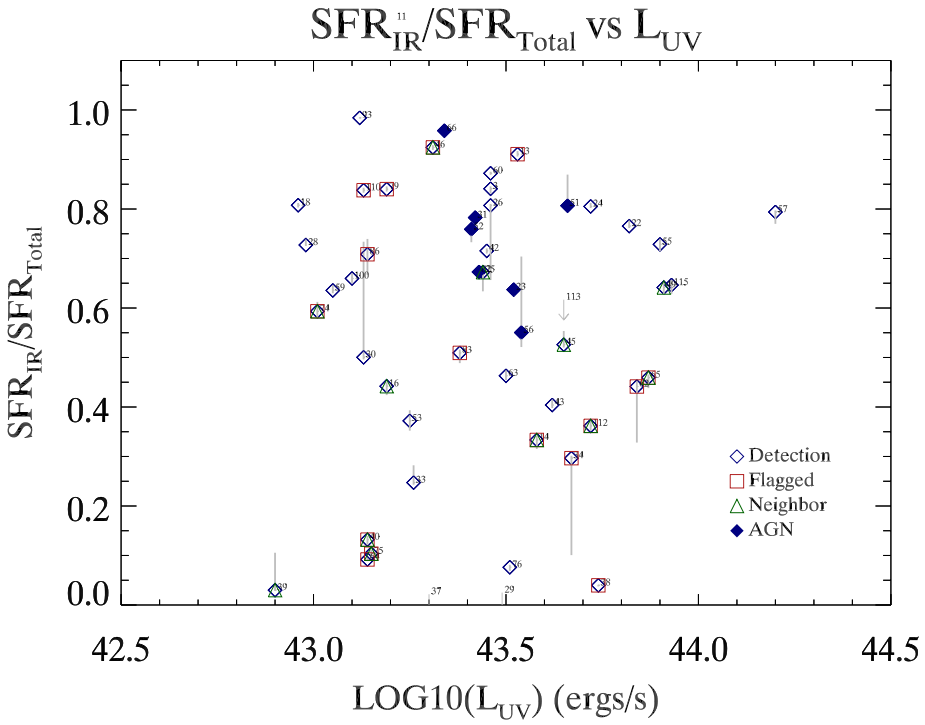

Figure F The ratio between SFR_{IR} and SFR_{Total}, against L_{UV}.

sample, the contribution of SFR_{IR} to SFR_{Total} is greater than 60%, and the median SFR_{IR} contribution is 64.6%. This is significant, because it indicates that even though some of the LAEs have very low dust attenuation, the contribution of SFR_{UV} alone is also not a good indicator of SFR_{Total}.

4.2.3 Dust Attenuation and UV Continuum Slope

Because dust attenuates each galaxy's UV light in a wavelength-dependent way (shorter wavelengths experience more attenuation), the UV continuum slope for each galaxy is expected to be related to the degree of dust attenuation for the galaxy. This is based upon the assumption that the native SED for a galaxy will be essentially flat for UV continuum emission, allowing the degree of "redness" seen in the UV spectrum to be an indicator for the degree of dust attenuation affecting each galaxy's spectrum. In this section, we will examine this relationship between dust attenuation and UV continuum

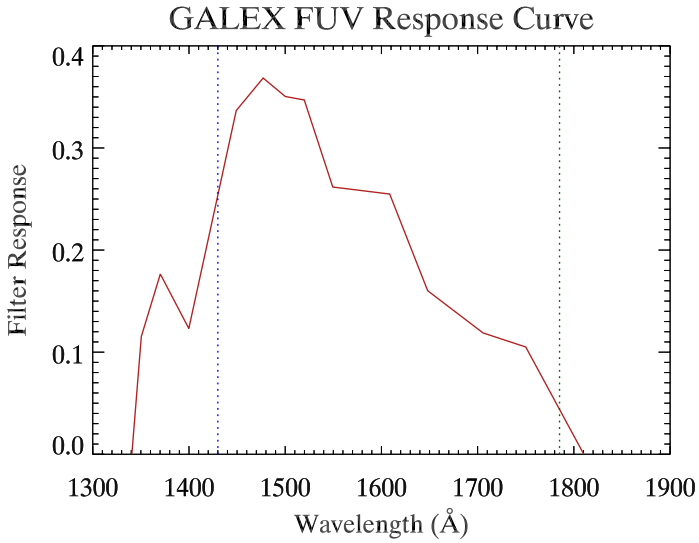

Figure G The response curve for the GALEX FUV filter, with $\lambda_{\rm obs}$ for Lyα emission line marked for the lowest-z (blue) and highest$-z$ (green) objects in our sample.

slope for our own sample of LAEs.

We will define the rest-frame UV continuum slope as β, where the shape of the UV continuum SED is described as a power law in the form $f_\lambda = \lambda^\beta$ (Kong et al. (2004)). We use the GALEX FUV and NUV channels to define β, but before calculating β we first correct for the contribution of the Lyα line to the measured FUV magnitude. As Figure G shows, for every galaxy in our sample, $\lambda_{\rm obs}$ for the the Lyα line falls within the FUV filter curve, altering the FUV magnitude and distorting the measured value of β.

We calculated the contribution of the Lyα line to the FUV filter, $(f_\lambda)_{\rm filt}$ using the following equation,

$$(f_\lambda)_{\rm filt} = \frac{\int f_\lambda \cdot \lambda \cdot {\rm response}(\lambda)\, d\lambda}{\int \lambda \cdot {\rm response}(\lambda)\, d\lambda} \qquad \text{(vi)}$$

integrating over the observed Lyα emission line, where we define f_λ as the observed Lyα line profile for a given galaxy, a Gaussian curve with its peak at $\mu = \lambda_{\rm obs}$ and $\sigma = ({\rm FWHM_{obs}}/2\sqrt{2\ \ln 2})$. We estimate $\rm FWHM_{obs}$ as 15 Å for all of the galaxies in our sample, because the sample from Cowie et al. (2011) consists only of LAEs with

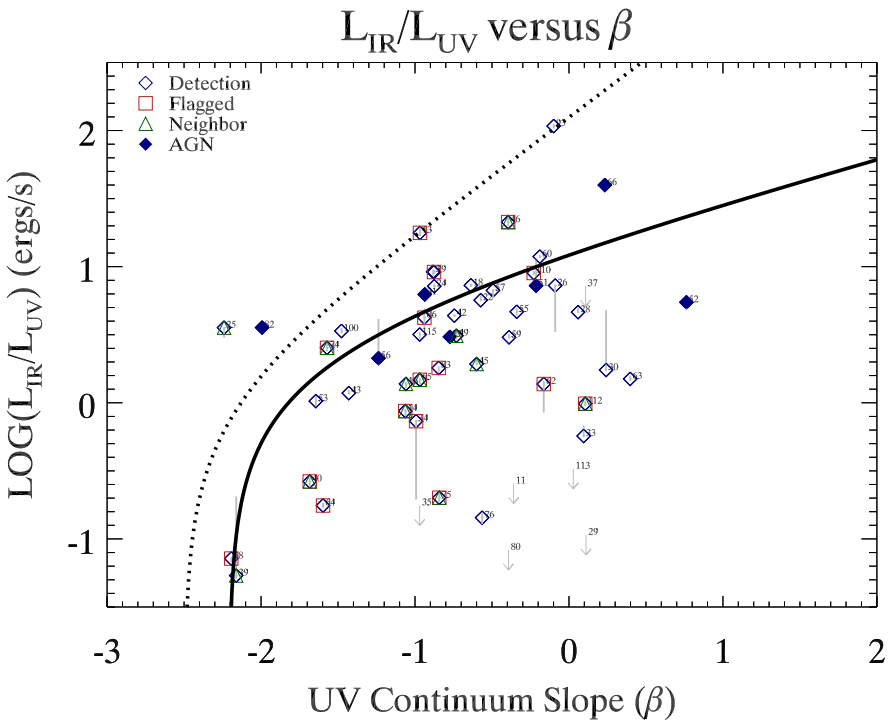

Figure H Dust attenuation against the UV continuum slope (β), obtained from GALEX NUV and FUV photometry in Cowie et al. (2011). Solid and dashed lines show the relations found for local normal star-forming galaxies (Boissier et al. (2007)) and starbursts(Kong et al. (2004)), respectively.

FWHM $<$ 15 Å. We define response(λ) as the response curve for the FUV filter.

Converting the FUV magnitude to a flux value, we found that the Lyα line contributed up to 19% of the measured flux in the FUV filter, with a median value of 4.8%. Subtracting this contribution from the measured flux and adjusting the FUV magnitude accordingly, we find that all of our values for β increase by some amount due to the increase in FUV magnitude. These increases in β fall in a range up to 0.525, with a median increase to β of 0.127. The resulting plot of β vs the $L_{\rm IR}/L_{\rm UV}$ ratio is shown in Figure H. The solid and dashed curves in the plot show the β vs dust attenuation relation derived for local normal star-forming (SF) galaxies (Boissier et al. (2007)) and starbursts (SBs) (Kong et al. (2004)), respectively.

In Figure H, we find some β values that are noticeably redder than those found in

Oteo et al. (2012). Several of our galaxies have $\beta > 0.0$, whereas only one of the galaxies in Oteo et al. (2012) falls in that range. We believe this is due to the fact that, in Oteo et al. (2012), Lyα line flux contributions were not subtracted from the flux measured by the FUV filter. Also, the fact that our sample consists of 48 LAEs, as opposed to the 23 LAEs examined in Oteo et al. (2012), means that we have a higher probability of seeing a wider range of β values. Likewise, our larger sample gives us 10 galaxies with $L_{\rm IR}<L_{\rm UV}$, and the dust attenuation covers a range that is wider by a full order of magnitude.

Some of the LAEs in our sample fall along the SF and SB curves, but most of the LAEs do not fall near either curve. This indicates that a single unique relation between the UV continuum slope and dust attenuation cannot be applied to LAEs at $z \sim 0.3$, so we cannot use β to recover the dust attenuation for the LAEs in our sample population. The assumption at the beginning of this section, i.e. that the native UV continuum slope would be essentially flat without dust attenuation, may not hold true for our sample of LAEs. It may be that the LAEs in our sample contain stellar populations of varying ages, so their native SEDs may yield values of β that do not follow the same predictable patterns of SF and SB galaxies, preventing us from using their UV continuum slope to recover their level of dust attenuation.

Chapter 5

Conclusions

We analyzed *Spitzer* data for a large sample of low-redshift Lyα-emitting galaxies discovered by GALEX, deriving their IR SEDs as well as determining their total bolometric $L_{\rm IR}$ SFR, dust extinction, and AGN fraction.

Using the Donley et al. (2012) AGN selection region in color-color space with our IRAC photometry, we determined that LAEs at $z \sim 0.3$ have an AGN fraction of $\approx 24\%$, which is consistent with the past results of Cowie et al. (2011) and Scarlata et al. (2009), who reported AGN fractions of $\approx 20\%$ and $\approx 17\%$, respectively.

We used χ^2 fitting along with the CE01 template SEDs to determine the total $L_{\rm IR}$ for our sample, finding that the galaxies ranged from $10^{8.05} L_\odot$ to $10^{11.57} L_\odot$, with a median $L_{\rm IR}$ value of $10^{10.39} L_\odot$.

From the $L_{\rm IR}$ values we calculated, we determined that $L_{\rm IR}$ and $L_{{\rm Ly}\alpha}$ do not appear to be correlated, unlike the high-$L_{\rm IR}$ Lyα-emitting objects examined by Colbert et al. (2006) and Nilsson & Møller (2009) This apparent correlation could be due to the small number of LAEs in their data samples, or, due to the fact that all of these objects are in the ULIRG range ($L_{\rm IR}/{\rm L}_\odot > 10^{12}$), they may be qualitatively different objects than those in our sample.

We found that the distribution of SFR values for our sample has a median value of 5.63 $M_\odot$ yr^{-1}, in agreement with the value of $\sim 6 M_\odot$ yr^{-1} found in Cowie et al. (2011). Also, we found that, although $SFR_{\rm IR}$ alone is not a good indicator of $SFR_{\rm Total}$ for our sample, most of the sample still has a contribution of $SFR_{\rm IR}$ to $SFR_{\rm Total}$ that is greater than 60%. This indicates that these galaxies have a significant amount of dust

extinction, and SFR_{UV} alone is also not a good indicator for SFR_{Total}.

From analyzing the relationship between dust extinction and the UV continuum slope for our sample, we found that LAEs do not follow the same curves predicted for SF or SB galaxies, indicating that LAEs at low redshift may experience more variation in their native UV spectra, making it impossible to recover their dust attenuation from their UV slope. This would suggest that LAEs may consist of stellar populations of varying ages, leading to more intrinsic variation in their UV slope.

References

Atek, H., Kunth, D., Hayes, M., Ostlin, G., Mas-Hesse, J. M. 2008, A&A, 488, 491

Atek, H., Kunth, D., Schaerer, D. et al. 2009, ArXive e-prints 0906.5349

Baldwin, J. A., Phillips, M. M., Terlevich, R. 1981, PASP, 93, 5

Barmby, P. et. al. 2008, ApJ, 642, 126

Boissier, S., et al. 2007, ApJS, 173, 524B

Bruzual, A. G. & Charlot, S. 1993, ApJ, 405, 538

Bruzual, G. & Charlot, S. 2003, MNRAS, 344, 1000

Caplan, J. & Deharveng, L. 1986, A&A, 155, 297

Cardelli, J. A., Clayton, G. C., Mathis, J. S. 1989, ApJ, 345, 245

Carter, B. J., Fabricant, D. G., Geller, M. J., Kurtz, M. J., & McLean, B. 2001, ApJ, 559,606

Charlot, S. & Fall, S. M. 1993, ApJ, 415, 580

Colbert, J., et al. 2006, ApJ, 637L, 89C

Chary, R. & Elbaz, D. 2001, ApJ, 556, 562C

Cowie, L.L., Barger, A.J., Hu, E.M., 2009, ArXive e-prints 0909.0031

Cowie, L.L., Barger, A.J., Hu, E.M. 2010, ApJ, 711, 928

Cowie, L.L., Barger, A.J., Hu, E.M., 2011, ApJ, 738, 136C

Deharveng, J.-M., Small, T., Barlow, T. A. et al. 2008, ApJ, 680, 1072

Dijkstra, M., Haiman, Z., & Spaans, M. 2006, ApJ, 649, 14

Donley, J., et al. 2012, AAS, 21922507D

Finkelstein, S. L., Rohads, J. E., Malhotra, S. et al. 2008, ApJ, 678, 655

Finkelstein, S. L., et al., 2009, ApJ, 700, 276

Finkelstein, S. L., et al., 2009, ApJ, ArXive e-prints 0906.4554

Gawiser, E., et al. 2006, ApJS, 162,1

Giavalisco, M., Koratkar, A., & Calzetti, D. 1996, ApJ, 466, 831

Hansen, M. & Oh, S. P. 2006, MNRAS, 367, 979

Hayes, M. et al. 2007, MNRAS, 382, 1465

Kauffmann, G. et al. 2003, MNRAS, 341, 33

Kennicutt, Robert C., Evans, Neal J. 2012, ARA&A, 50, 531K

Kewley, L. J. et al. 2001, ApJ, 556, 121

Kong, X., et at. 2004, MNRAS, 349, 769K

Lacy, M., et al. 2007, ApJ, 133, 186

Laursen, P. & Sommer-Larsen, J. 2007, ApJ, 657, L69

Lee, N., LeFloc'h, E., Sanders, D.B., 2011, AAS, 21733538L

Malhotra, S. & Rhoads, J. 2006, ApJ, 647L, 95M

Mathis, J. S. 1972, ApJ, 176, 651

Miller, C. J. et al. 2003, ApJ, 597, 142

Miralda-Escude, J. & Rees, M. 1998, ApJ, 497, 21M

Natta, A. & Panagia, N. 1984, ApJ, 287, 228

Neufeld, D. A. 1990, ApJ, 350, 216

Neufeld, D. A. 1991, ApJ, 370, L85

Nilsson, K.K. & Møller, P. 2009, A&A, 508L, 21N

Oke, J. B. & Gunn, J. E. 1982, PASP, 94, 586

Ostlin, G. et al. 2008, ArXiv e-prints

Osterbrock, D.E. & Ferland, G.J., Astrophysics of Gaseous Nebulae and Active Galactic Nuclei, 2006

Oteo, I. et al. 2012, ApJ, 751, 139O

Panagia, N. & Ranieri, M. 1973a, A&A, 24, 219

Panagia, N. & Ranieri, M. 1973b, in Les Nebuleuses Planetaires, 275280

Pengelly, R. M. 1964, MNRAS, 127, 145

Polletta, M., et al. 2007, ApJ, 663, 81

Scarlata, C., et. al. 2009, ApJ, 704, L98

Stern, D., et. al. 2006, ApJ, 631, 163

Valls-Gabaud, D. 1993, ApJ, 419, 7

Verhamme, A., Schaerer, D., & Maselli, A. 2006, A&A, 460, 397

York, D. G. et al. 2000, AJ, 120, 1579

Appendix A

Spitzer Images and SEDs

Table A.1: – Stamps and SED Fits (Detected in All Four IRAC Bands). Green circles indicate the selection region for each object's IR counterpart, with a radius of 3" for IRAC and 6" for MIPS. GALEX coordinates are marked in blue, and the coordinates of the nearest SExtractor-defined infrared source are marked in red.

#	IRAC1	IRAC2	IRAC3	IRAC4	MIPS1	SED Fit
3	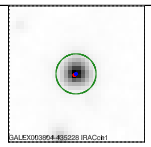	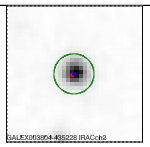	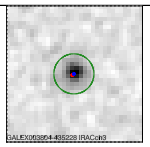	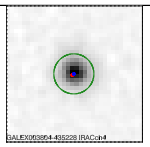	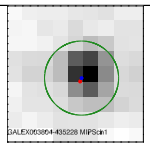	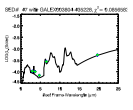
4	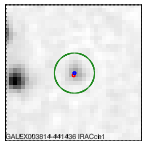	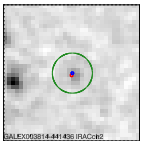	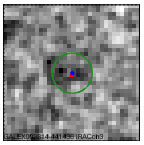	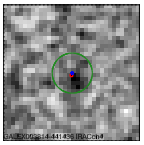	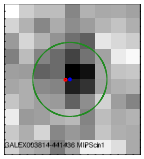	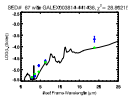
5	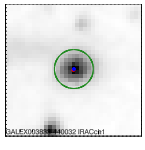	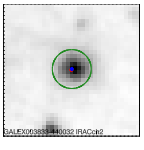	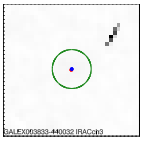	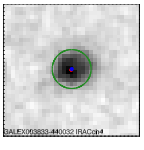	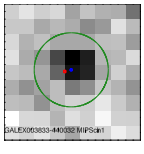	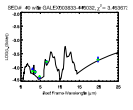

Continued on next page

Table A.1 – Stamps and SED Fits (Detections) – *Continued from previous page*

#	IRAC1	IRAC2	IRAC3	IRAC4	MIPS1	SED Fit
7	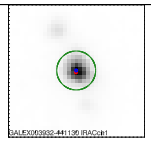	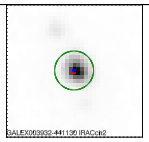	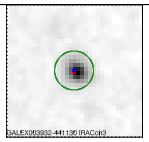	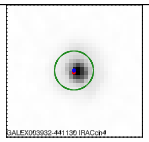	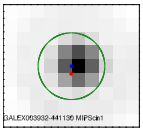	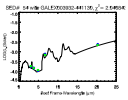
8	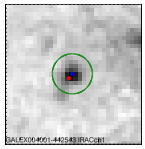	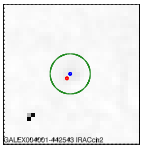	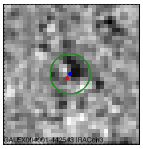	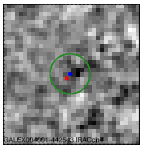	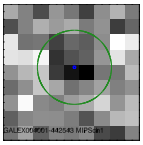	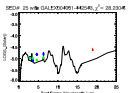
15	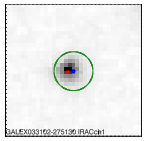	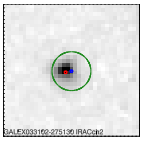	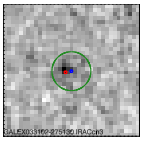	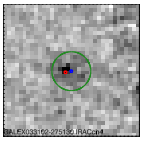	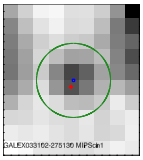	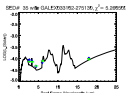
18	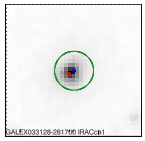	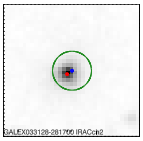	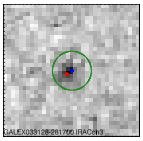	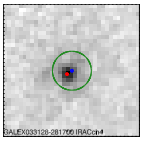	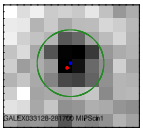	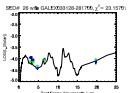
20	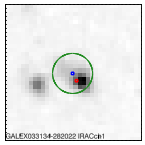	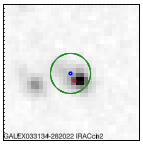	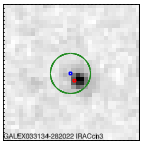	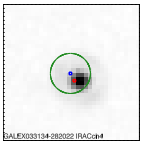	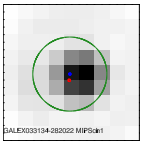	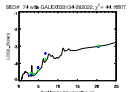
22	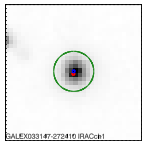	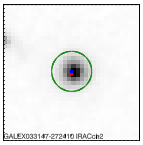	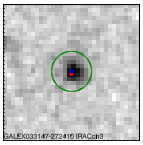	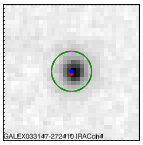	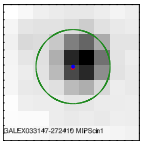	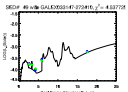
23	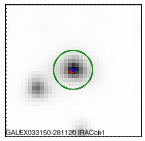	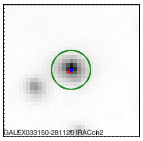	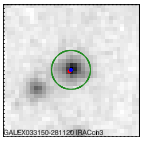	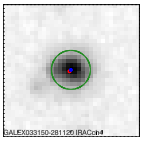	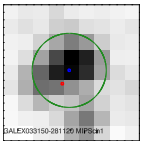	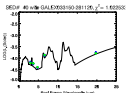
24	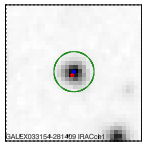	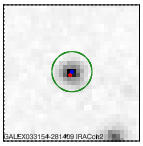	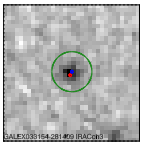	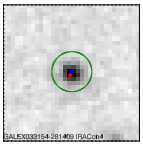	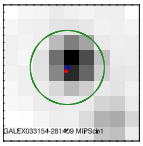	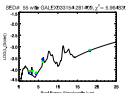
25	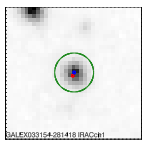	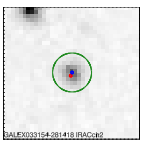	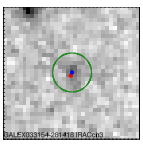	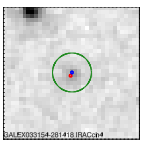	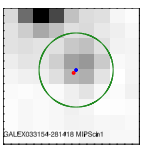	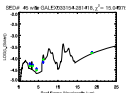

Continued on next page

Table A.1 – Stamps and SED Fits (Detections) – *Continued from previous page*

#	IRAC1	IRAC2	IRAC3	IRAC4	MIPS1	SED Fit
26	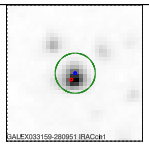	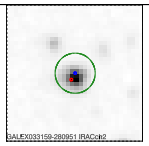	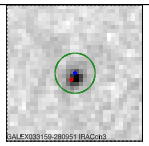	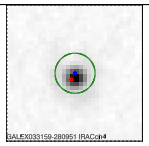	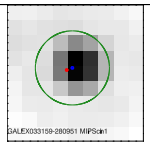	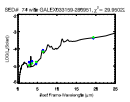
28	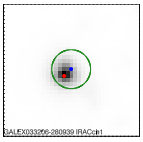	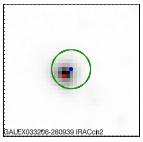	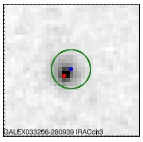	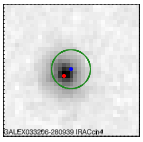	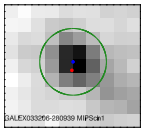	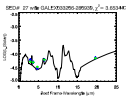
30	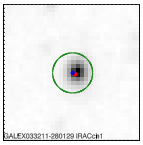	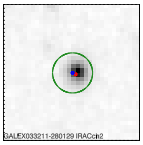	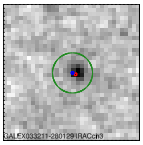	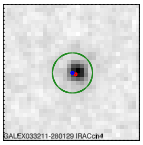	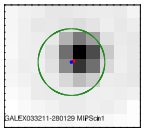	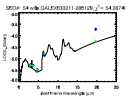
31	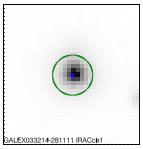	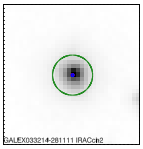	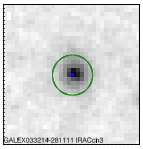	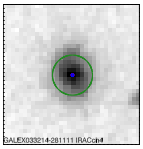	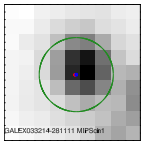	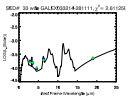
32	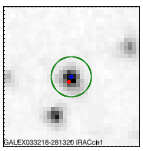	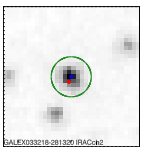	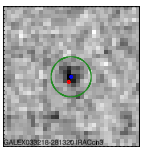	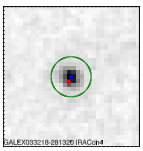	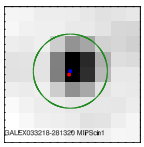	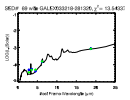
33	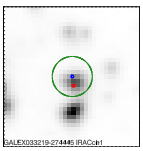	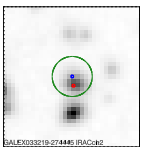	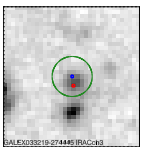	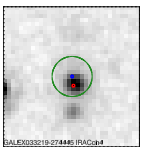	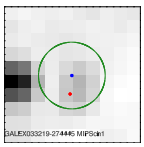	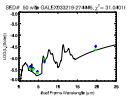
34	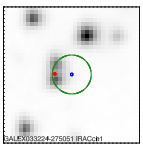	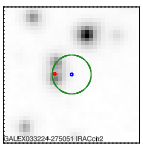	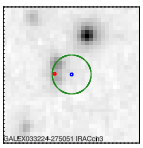	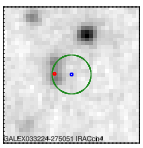	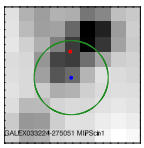	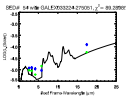
35	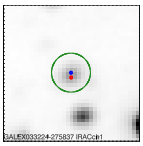	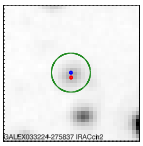	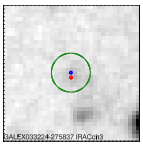		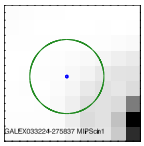	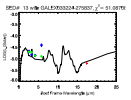
38	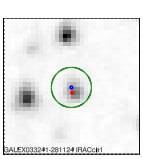	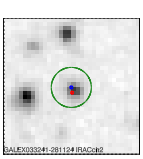	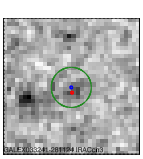	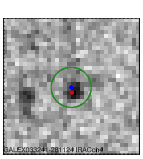	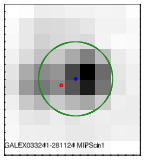	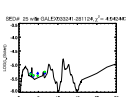

Continued on next page

Table A.1 – Stamps and SED Fits (Detections) – *Continued from previous page*

#	IRAC1	IRAC2	IRAC3	IRAC4	MIPS1	SED Fit
40	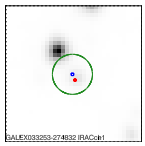	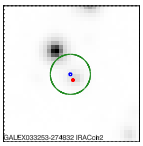	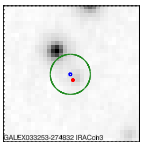	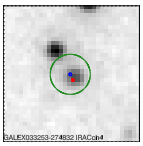	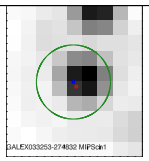	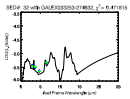
42	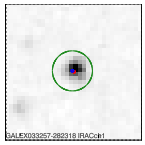	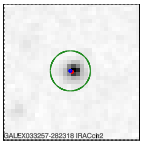	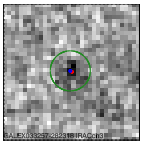	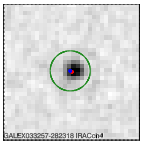	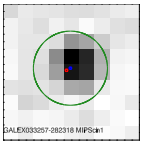	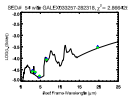
43	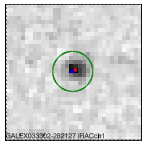	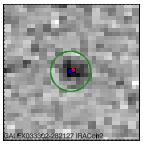	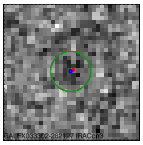	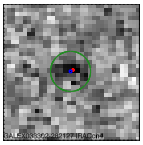	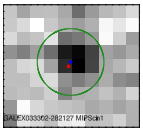	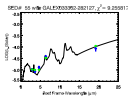
44	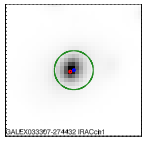	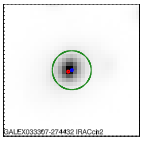	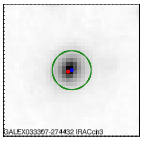	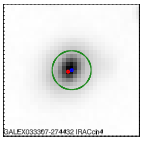	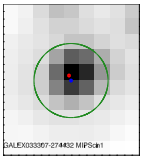	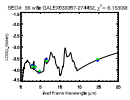
45	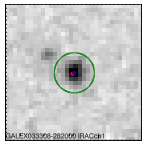	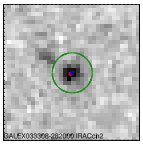	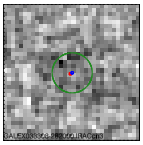	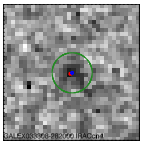	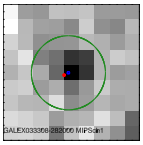	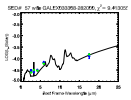
49	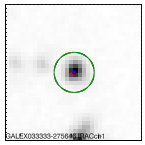	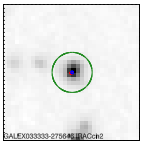	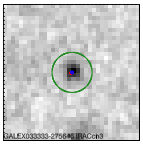	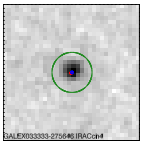	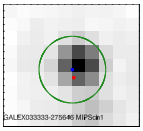	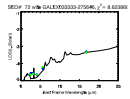
51	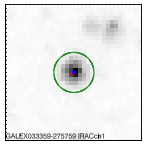	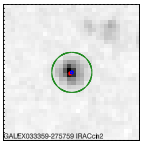	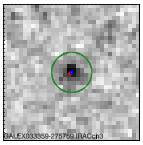	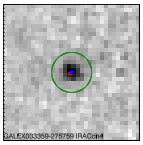	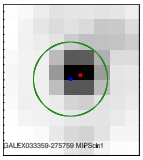	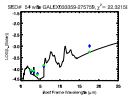
52	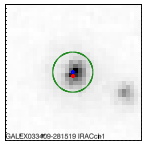	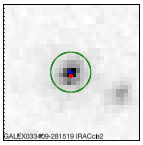	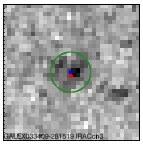	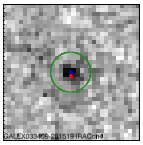	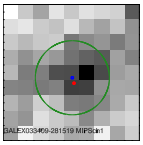	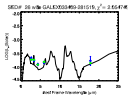

Continued on next page

Table A.1 – Stamps and SED Fits (Detections) – *Continued from previous page*

#	IRAC1	IRAC2	IRAC3	IRAC4	MIPS1	SED Fit
55	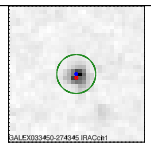	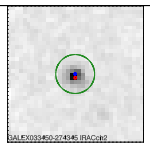	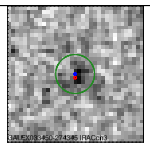	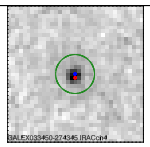	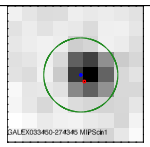	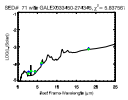
56	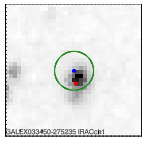	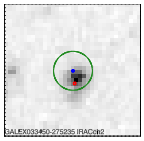	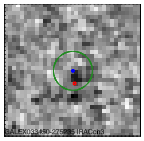	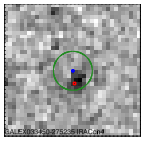	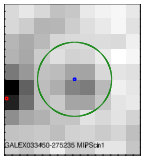	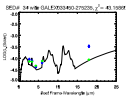
57	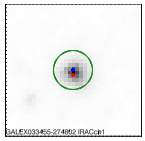	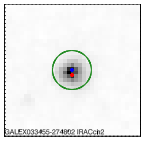	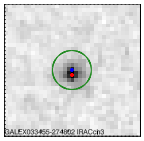	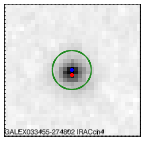	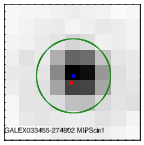	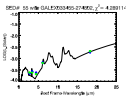
59	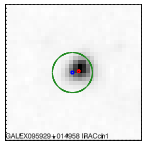	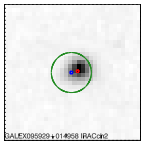	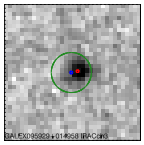	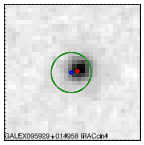	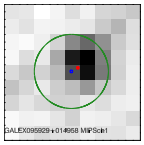	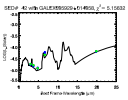
60	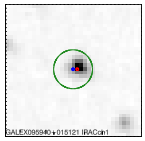	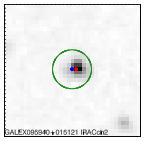	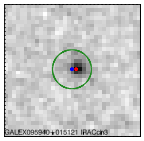	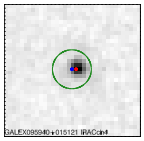	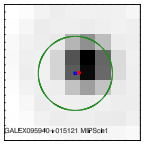	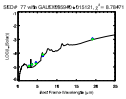
62	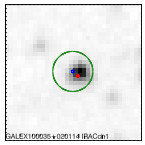	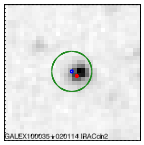	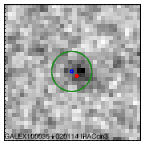	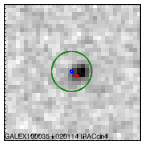	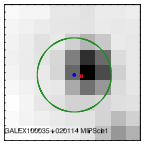	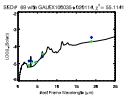
64	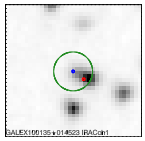	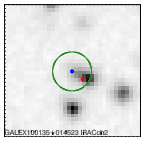	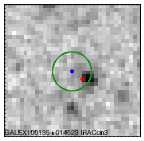	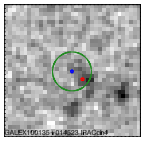	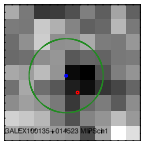	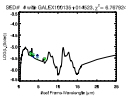
65	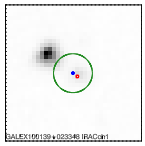	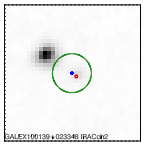	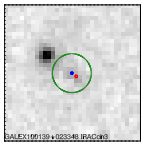	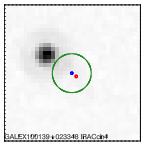	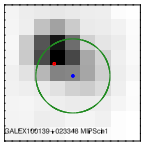	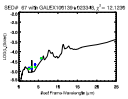
66	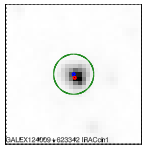	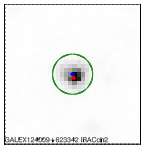	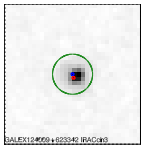	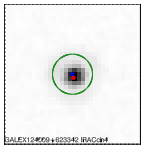	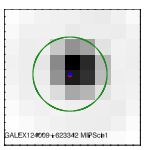	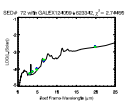

Continued on next page

Table A.1 – Stamps and SED Fits (Detections) – *Continued from previous page*

#	IRAC1	IRAC2	IRAC3	IRAC4	MIPS1	SED Fit
69	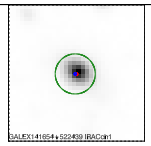	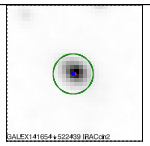	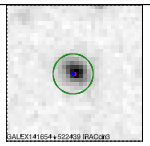	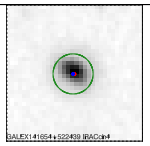	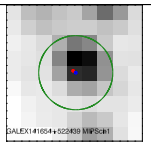	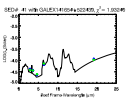
73	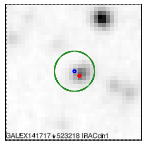	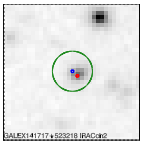	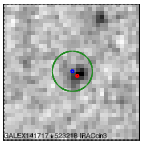	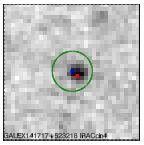	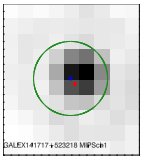	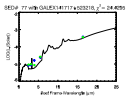
76	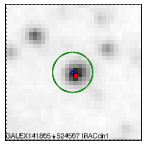	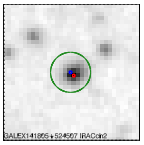	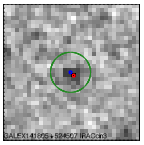	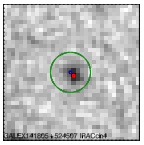	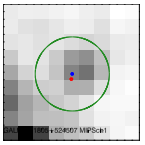	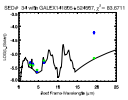
82	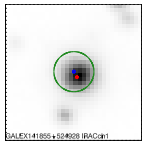	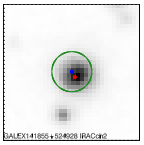	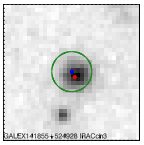	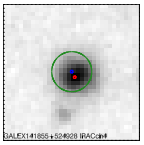	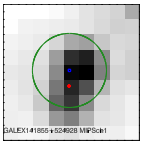	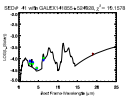
83	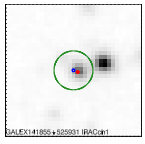	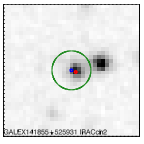	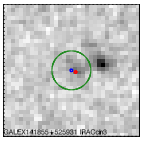	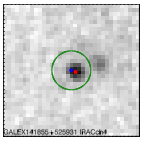	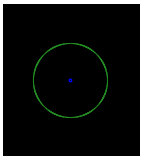	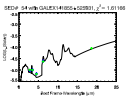
87	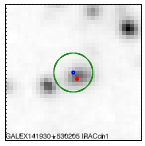	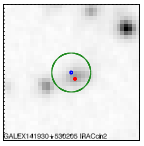	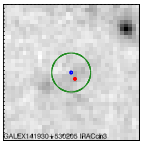	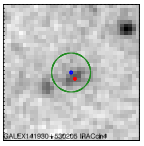	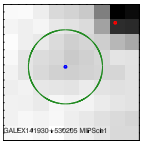	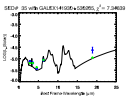
93	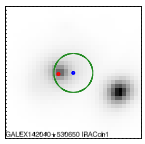	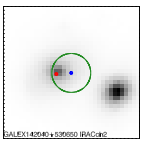	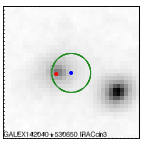	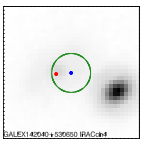	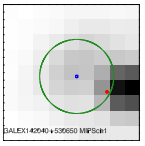	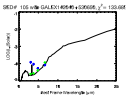
100	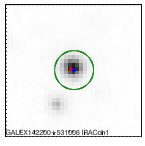	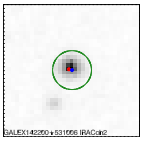	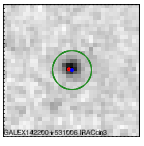	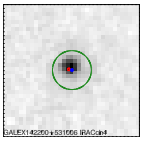	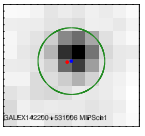	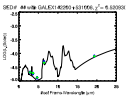
111	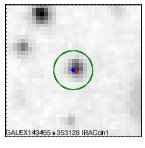	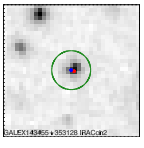	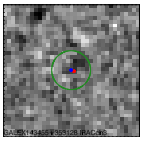	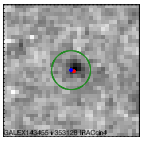	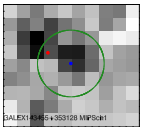	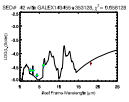

Continued on next page

Table A.1 – Stamps and SED Fits (Detections) – *Continued from previous page*

#	IRAC1	IRAC2	IRAC3	IRAC4	MIPS1	SED Fit
118	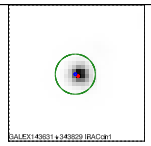	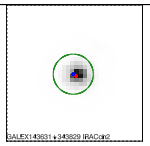	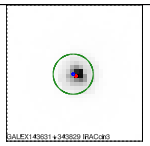	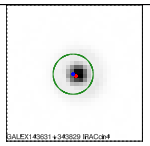	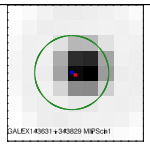	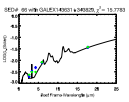
119	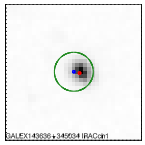	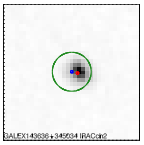	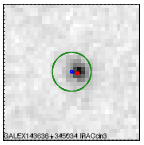	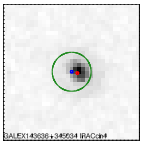	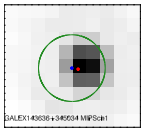	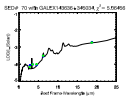
123	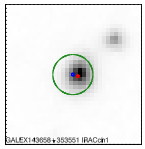	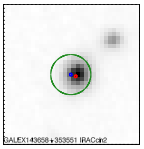	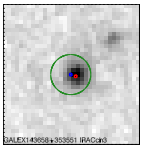	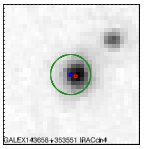	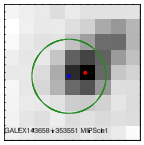	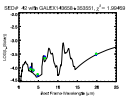
126	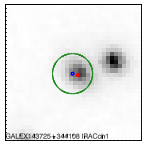	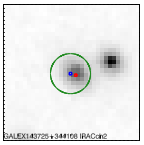	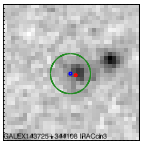	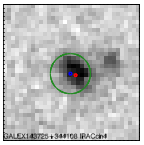	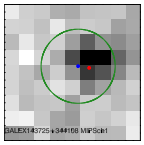	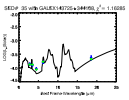
127	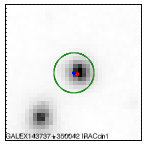	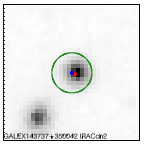	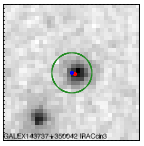	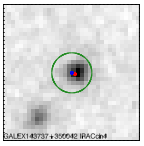	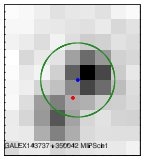	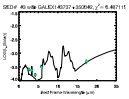
130	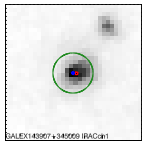	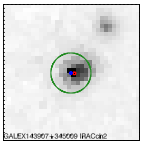	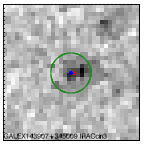	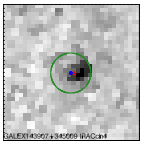	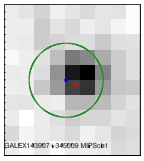	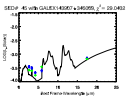
137	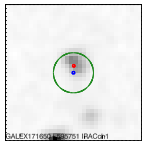	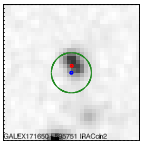	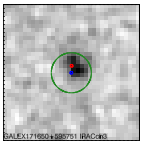	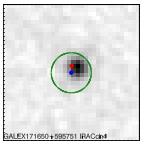	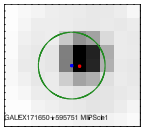	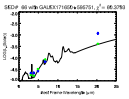

Table A.2: – Stamps and SED Fits (Limits in some IRAC Bands). Green circles indicate the selection region for each object's IR counterpart, with a radius of 3" for IRAC and 6" for MIPS. GALEX coordinates are marked in blue, and the coordinates of the nearest SExtractor-defined infrared source are marked in red.

#	IRAC1	IRAC2	IRAC3	IRAC4	MIPS1	SED Fit
2	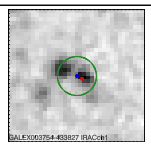	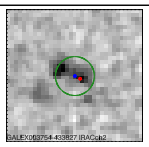	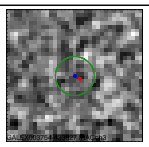	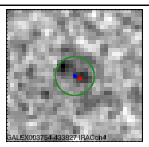	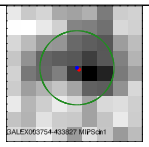	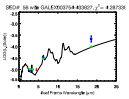
6	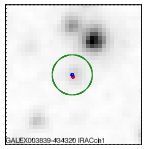	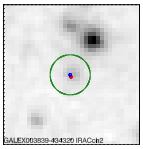	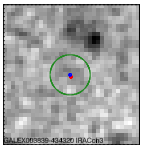	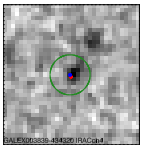	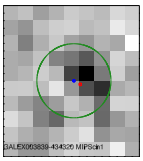	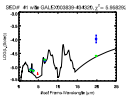
14	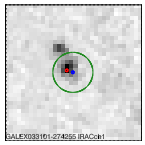	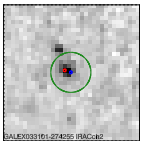	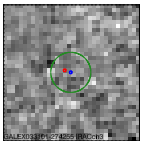	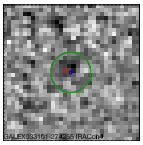	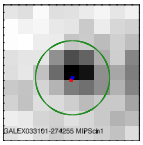	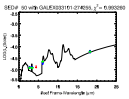
16	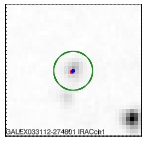	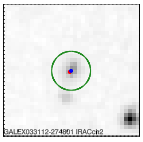	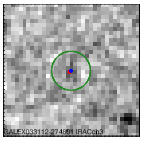	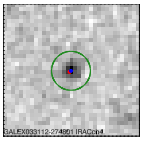	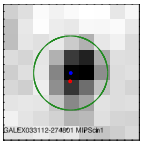	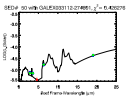
39	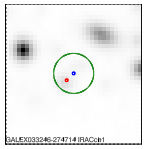	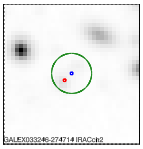	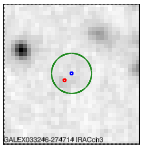	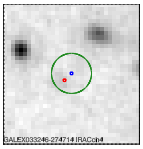	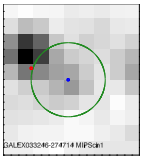	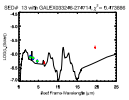
53	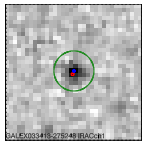	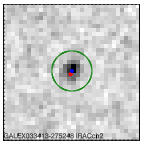	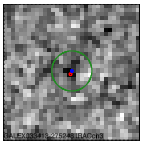	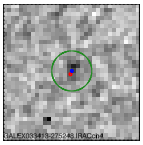	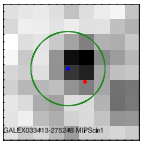	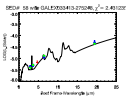
63	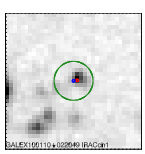	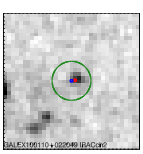	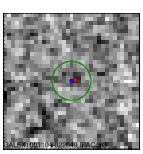	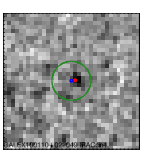	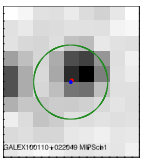	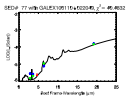

Continued on next page

Table A.2 – Stamps and SED Fits (Limits) – *Continued from previous page*

#	IRAC1	IRAC2	IRAC3	IRAC4	MIPS1	SED Fit
74	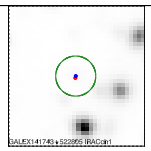	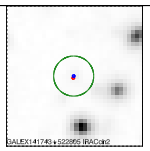	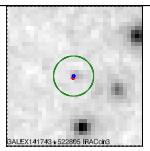	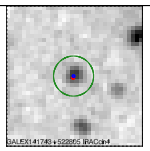	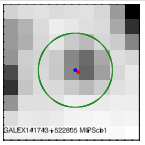	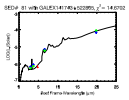
75	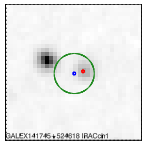	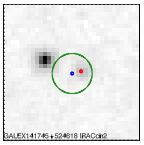	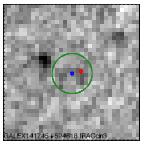	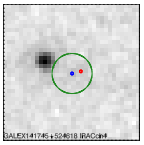	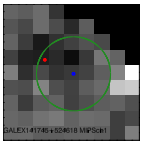	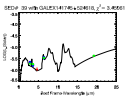
77	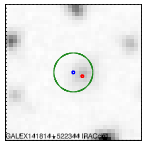	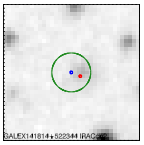	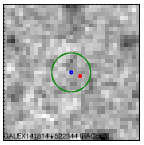	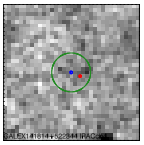	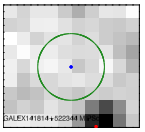	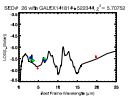
79	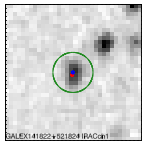	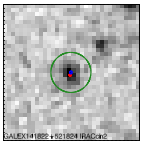	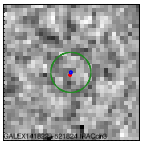	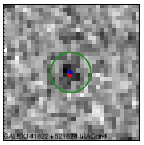	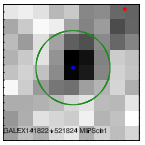	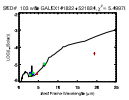
110	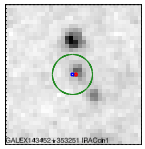	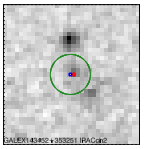	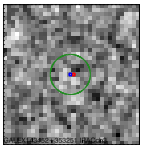	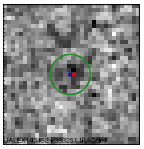	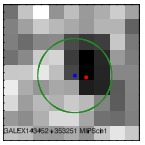	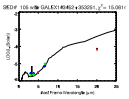
113	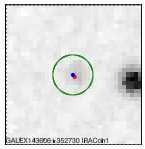	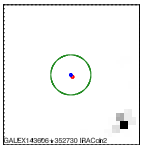	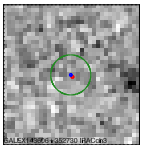	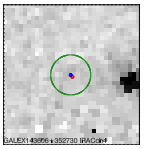	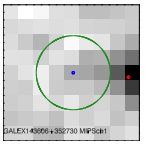	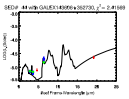
116	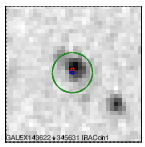	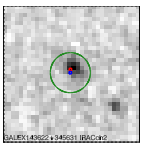	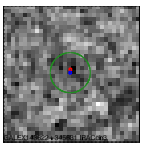	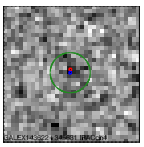	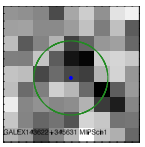	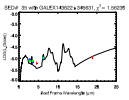
124	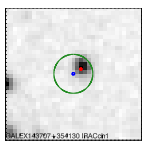	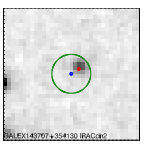	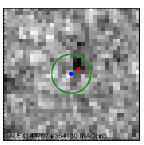	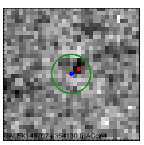	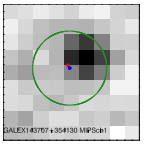	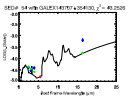
125	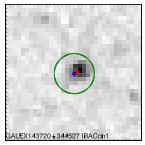	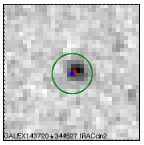	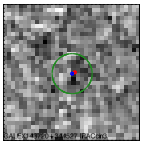	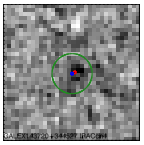	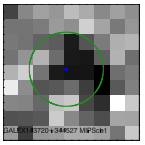	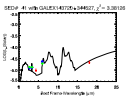

Continued on next page

Table A.2 – Stamps and SED Fits (Limits) – *Continued from previous page*

#	IRAC1	IRAC2	IRAC3	IRAC4	MIPS1	SED Fit
129	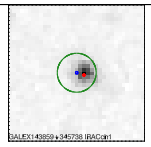	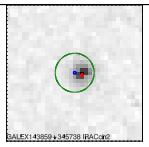	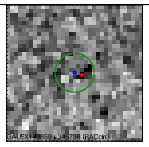	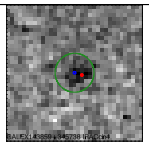	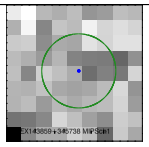	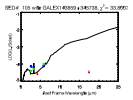
133